PERGAMON

International Journal of Multiphase Flow 28 (2002) 665–697

International Journal of Multiphase Flow

www.elsevier.com/locate/ijmulflow

Dispersion in multiphase flow through porous media

S. Bekri, P.M. Adler *

IPGP, Tour 24, 4 Place Jussieu, 75252 Paris Cedex 05, France

Received 18 February 2001; received in revised form 30 November 2001

Abstract

Dispersion of a passive solute in two phase flow through porous media has been studied by combining three tools, namely reconstruction of porous media, Immiscible Lattice Boltzmann algorithm and random walks. Plane Poiseuille flow has been solved analytically and it provides a useful comparison for the random walk code. The influence of the Péclet number, of the water saturation and of the partition coefficient has been determined for two different samples. Overall correlations are proposed to cover the variations of the two first parameters.

Keywords: Two phase flow; Porous media; Dispersion; Immiscible lattice gas; Random walk; Partition coefficient; Kinetic coefficient

1. Introduction

The study of dispersion of a passive tracer in multiphase flow through a porous medium is a difficult topic which has not received much attention in the past though it has a lot of practical and fundamental interest. For instance, tracer analysis is currently used between wells to gain a better understanding of the underground structure and of the flow pattern.

The contributions to dispersion studies in multiphase flow through porous media are not very numerous to the best of our knowledge. The first one is Sahimi et al. (1982) which was later summarized by Sahimi et al. (1983). Sahimi (1995) reviewed the early numerical contributions in networks by Salter and Mohanty (1982), Sahimi et al. (1986) and Sahimi and Imdakm (1988). Delshad et al. (1985) conducted a thorough experimental study in Berea sandstones and sandpacks with two and three phase flows; this paper summarizes some of the previous experimental studies; it shows that dispersion is a strong function of the preferential phase where the tracer is,

* Corresponding author. Tel.: +33-1-4427-2428; fax: +33-1-4427-3373.
E-mail address: adler@ipgp.jussieu.fr (P.M. Adler).

0301-9322/02/$ - see front matter
PII: S0301-9322(01)00089-1

of the saturation, of the porous medium and of surface tension; the data are analyzed in terms of dispersivity which is the dispersion coefficient divided by the interstitial velocity. Recently, Chella et al. (1998) investigated some theoretical aspects and performed some numerical applications in elementary geometries with fixed interfaces.

Another source of results comes from hydrology and many theoretical, numerical and experimental investigations were carried out in the seventies in unsaturated porous media; for instance, Smiles et al. (1978) used soils and De Smedt and Wierenga (1979) glass beads. Though it is limited to diffusion, it is useful to cite the experimental study of Conca and Wright (1990) in unsaturated gravel. Finally, Haga et al. (1999) conducted detailed tracer response experiments on a packed bed of glass beads; the longitudinal dispersion coefficient was found to be proportional to the product of the Péclet number and of the power -3.1 of the water saturation.

This paper is organized as follows. Section 2 is devoted to a short presentation of the basic tools which are necessary for the determination of the dispersion tensor at the local scale. First, the pore space is determined by means of the method of reconstructed media. Second, the instantaneous phase distribution and velocity fields are obtained by means of an Immiscible Lattice Boltzmann model. Third, the dispersion tensor is obtained by the random walk technique.

The simple case of plane Poiseuille flow is described in Section 3. This is the only geometry where an analytical solution can be obtained. It is successfully compared with the numerical results derived by random walks.

The general situation of reconstructed media is addressed in Section 4. Results for two sets of porous media, three values of the partition coefficient, three values for the Péclet number and four values of water saturation are presented and discussed. Asymptotic values for long times of the longitudinal dispersion coefficients are obtained by the Levenberg–Marquardt method. A few overall correlations in terms of the Péclet number and of the water saturation are proposed.

2. General

Let us start by a general presentation of the determination of the dispersion tensor in two phase flow; in most cases, the two fluids are oil and water denoted by the subscripts o and w. Consider a solute which is diffusing while it is convected by a two phase flow; this solute has different diffusion coefficients D_o and D_w in the phases; moreover, it is characterized by a partition coefficient K which is defined as being the ratio at equilibrium of the concentrations c_o and c_w

$$K = \frac{c_o}{c_w} \tag{1}$$

The determination of the dispersion tensor necessitates three tools which are going to be presented in this section. First, a realistic representation of the porous medium is needed; it is obtained by our classical technique of reconstructed porous media (Adler et al., 1990). Second, the simultaneous flux of the two phases through the porous medium requests the resolution of the Navier–Stokes equations in each phase supplemented by adequate boundary conditions at the liquid–liquid interface and at the solid surface. This is achieved by using our Immiscible Lattice Boltzmann code (Gunstensen, 1992; Ginzbourg and Adler, 1995). Third, convection–diffusion of the Brownian solute is described by a convection–diffusion equation; except for the case of Poiseuille flow, this will be solved by a random walk algorithm (Sallès et al., 1993).

In this section, we shall briefly summarize these three tools. For sake of completeness, the reader is referred to references with more complete presentations.

2.1. Reconstruction of porous media

The general principle of this technique consists of measuring statistical quantities on the real material and to generate media with the same average properties. Here, these measurements are performed on the digitized images of thin sections. Each section is described by a $L_x \times L_y$ matrix of square binary pixels, which take the values 0 or 1 in the solid or pore phases, respectively. The physical dimension of these pixels is denoted by p. This representation is a discrete definition of the phase function

$$Z(\boldsymbol{r}) = \begin{cases} 1 & \text{if } \boldsymbol{r} \text{ belongs to the pore space} \\ 0 & \text{otherwise} \end{cases} \tag{2}$$

where $\boldsymbol{r}$ denotes the position with respect to an arbitrary origin.

The porosity ϵ and the correlation $R_z(\boldsymbol{u})$ can be defined by the statistical averages (which are denoted by overbars)

$$\epsilon = \overline{Z(\boldsymbol{r})} \tag{3}$$

$$R_Z(\boldsymbol{u}) = \frac{\overline{(Z(\boldsymbol{r}) - \epsilon) \cdot (Z(\boldsymbol{r} + \boldsymbol{u}) - \epsilon)}}{\epsilon(1 - \epsilon)} \tag{4}$$

For isotropic materials, R_Z is a function of the modulus of the lag $u = \|\boldsymbol{u}\|$ only, $R_Z(\boldsymbol{u}) = R_Z(u)$. Otherwise, the correlations for $\boldsymbol{u}$ parallel to the x- and y-axes are denoted R_{Zx} and R_{Zy}, respectively. Notice that $\epsilon(1 - \epsilon)$ in Eq. (4) equals var(Z) since $Z^n(\boldsymbol{r}) = Z(\boldsymbol{r})$.

These two quantities can be measured on a thin section by image analysis. The porosity is obtained by averaging. The increment u was varied by steps of one pixel. The correlation length $\mathscr{L}$ is defined as the integral of the correlation function

$$\mathscr{L} = \int_0^\infty R_Z(u)\,\mathrm{d}u \tag{5}$$

For anisotropic materials, $\mathscr{L}_x$ and $\mathscr{L}_y$ are defined accordingly from R_{Zx} and R_{Zy}.

The reconstruction method of three-dimensional random media consists of generating three-dimensional random porous media with a given porosity ϵ and a given correlation function; the medium is homogeneous and isotropic, but this last property is not essential. This technique has been fully described by Adler et al. (1990); recent developments have been summarized by Adler and Thovert (1998) and Thovert et al. (2001).

For practical purposes only, the porous medium is constructed in a discrete manner. It is considered to be composed of N_c^3 small cubes, each of the same size a. These elementary cubes are filled either with void or with solid. Moreover, the generated samples are unit cells of infinite spatially periodic media, a feature which will be convenient for the determination of the transport properties.

2.2. Two-phase flow (immiscible lattice Boltzmann models)

The motion of each fluid phase is computed with a classical Immiscible Lattice Boltzmann code (often denoted by the initials ILB) which was originated by Gunstensen (1992). It consists of Boltzmann equations supplemented by perturbation of populations near the interface in order to introduce surface tension; the separation of phases is performed in the same manner as in ILG models.

The algorithm has been thoroughly described by Ginzbourg and Adler (1995). It can be briefly summarized as follows. It is divided into five major steps. In the first step, the fields at time t such as the densities and the velocities are derived. In the second step, the collisions of the total populations are calculated by means of the Boltzmann equations. In the third step, surface tension is introduced and the color gradient is determined. In the fourth step, the total population is recolored in order to separate the two populations. Finally, propagation of the populations is achieved.

The wetting properties can be implemented in a very flexible way in ILB codes. Each surface element which belong to S_p is given an arbitrary color; this corresponds to the fact that the surface element is wetted by the phase of the same color. Hence, each element can be colored independently of its neighbors.

At a time t_i, one can compute the spatial averages of the velocities of each phase $\overline{\mathbf{v}}_k$, namely the seepage velocity. The instantaneous relative permeability $K_{rk}(t_i)$ of the phase k is defined by

$$\overline{\mathbf{v}}_k(t_i) = -\frac{K_{rk}(t_i)K}{\mu_k}\overline{\nabla p} \tag{6}$$

where K is the absolute permeability.

The instantaneous capillary pressure is defined as the instantaneous spatial average difference in pressure of the two phases

$$P_c(t_i) = P_1(t_i) - P_2(t_i) \tag{7}$$

where 1 and 2 are the non-wetting and the wetting phases, respectively. It can in some cases for very low velocities be taken as a function of the water saturation. Furthermore, the capillary number is defined as

$$C_k = \frac{\mu_k|\overline{\mathbf{v}}_k|}{\sigma} \tag{8}$$

In the results from the Lattice–Boltzmann simulation the relative permeabilities, the capillary pressure and the capillary numbers are calculated for a series of $\mathcal{N}$ times t_i. The time averages values are indicated by brackets $\langle\ \rangle$; the average is a moving average in the sense that only the last $\mathcal{N}$ points are used. For instance, the average real permeabilities are given by

$$\langle K_{rk}\rangle = \frac{1}{\mathcal{N}}\sum_{i=1,\mathcal{N}} K_{rk}(t_i) \tag{9}$$

Usually, these average relative permeabilities are assumed to be functions only of the saturation of water S_w (or equivalently of $S_o = 1 - S_w$)

$$\langle K_{rk} \rangle = K_{rk}(S_w) \tag{10}$$

2.3. Convection–diffusion in two phase flow

2.3.1. Theoretical background in single phase flow

Dispersion is motion under the simultaneous influence of convection and diffusion. A complete analysis of this question can be found in Brenner (1980), Adler (1992) and Sallès et al. (1993). Consider Brownian particles injected into a fluid and for sake of simplicity, let us start with the simple case of a single phase fluid which is incompressible. The concentration field of the particles is governed by the convection–diffusion equation

$$\frac{\partial c}{\partial t} + \boldsymbol{v} \cdot \nabla c - D\nabla^2 c = 0 \tag{11}$$

where c is the local solute concentration, $\boldsymbol{v}$ the local velocity, and D the diffusion coefficient.

Alternatively, one can consider the particles individually; let $\boldsymbol{r}_i(t)$ be the position of particle i. One can define the first and second moments of the population of particles

$$\boldsymbol{M}_1 = \langle \boldsymbol{r} \rangle \tag{12a}$$

$$\boldsymbol{M}_2 = \langle \boldsymbol{r}\boldsymbol{r} - \langle \boldsymbol{r} \rangle \langle \boldsymbol{r} \rangle \rangle \tag{12b}$$

In these formulae, $\langle \cdot \rangle$ denotes a statistical average over the Brownian particles; for instance,

$$\langle \boldsymbol{r} \rangle = \frac{1}{N} \sum_{i=1}^{N} \boldsymbol{r}_i(t) \tag{12c}$$

where N is the total number of particles. The physical meaning of these two moments is clear; the first one corresponds to the center of gravity of the cloud of particles, the second to the square of the diameter of this cloud.

Hence, the time derivative of $\boldsymbol{M}_1$ corresponds to the velocity of the centre of gravity of the cloud for sufficiently long times; by analogy with the standard Brownian motion, the time derivative of $\boldsymbol{M}_2$ corresponds to the dispersion tensor $\boldsymbol{D}^*$, again for sufficiently long times. More precisely,

$$\lim_{t\to\infty} \frac{\mathrm{d}\boldsymbol{M}_1}{\mathrm{d}t} = \overline{\boldsymbol{v}}_c^* \tag{13a}$$

$$\lim_{t\to\infty} \frac{1}{2} \frac{\mathrm{d}\boldsymbol{M}_2}{\mathrm{d}t} = \boldsymbol{D}^* \tag{13b}$$

These two quantities are of crucial importance since they are the ones which appear in the large scale transport equation.

$\overline{\boldsymbol{v}}_c^*$ is called the mean velocity vector of the tracer particle which is, for a single phase flow without reaction, equal to the interstitial velocity $\overline{\boldsymbol{v}}^*$ and related to the seepage velocity $\overline{\boldsymbol{v}}$ by

$$\overline{\boldsymbol{v}}_c^* = \overline{\boldsymbol{v}}^* = \frac{\overline{\boldsymbol{v}}}{\varepsilon} \tag{14}$$

The dispersion tensor is a symmetric positive tensor. For isotropic media, where flow is parallel to the x-axis, $\boldsymbol{D}^*$ can be decomposed into its parallel and perpendicular components

$$\boldsymbol{D}^* = \begin{Bmatrix} D^*_{\parallel} & 0 & 0 \\ 0 & D^*_{\perp} & 0 \\ 0 & 0 & D^*_{\perp} \end{Bmatrix} \tag{15}$$

In single phase flow, the dispersion tensor is not usually determined by the random walk technique which is very expensive numerically. Rather the so called $\boldsymbol{B}$-equation is used where $\boldsymbol{B}$ is a vector field solution of a stationary convection–diffusion equation with a second member (cf. Brenner, 1980).

Dispersion is dependent on many parameters. The relative influence of convection versus diffusion greatly affects the magnitude of the dispersion tensor. The convection/diffusion ratio is represented by the Péclet number where

$$Pe = \frac{|\overline{\boldsymbol{v}}^*| l}{D} \tag{16}$$

The Péclet number can be varied by altering the interstitial velocity $|\overline{\boldsymbol{v}}^*|$, or the diffusion coefficient D. In this study, the local velocity will be generally held constant and the Péclet number will be fixed by the diffusion coefficient.

2.3.2. Dispersion in multiphase flow

In multiphase flow, the problem is more complex than in single phase flow since the configuration of the phases is not constant with time. The technique of the $\boldsymbol{B}$-equation could be adapted to such a situation, but numerical difficulties would be created by the simultaneous use of the ILB code and of a finite volume code. In contrast, the random walk method is relatively easier to implement though it is computationally expensive.

Physically, the tracer is characterized by two diffusion coefficients D_{w} and D_{o} in water and oil, respectively. Moreover, in a state of thermodynamic equilibrium, the concentrations of particles in the two phases are generally different one from another. This concentration ratio is equal to the partition coefficient K. This dimensionless constant representing the ratio of the number of Brownian particles in oil to the number of Brownian particles in water, can be expressed by Eq. (1).

However, macroscopic quantities such as the moments of the particle populations, the mean solute velocity $\overline{\boldsymbol{v}}^*_{\mathrm{c}}$ and the dispersion tensor $\boldsymbol{D}^*$ can be defined exactly as for single phase flow, i.e., according to Eqs. (12a)–(13b). Hence, because of the partition coefficient and of the complex nature of the flow, $\overline{\boldsymbol{v}}^*_{\mathrm{c}}$ is definitively different from the average velocity.

In multiphase flows, the overall interstitial velocity $\overline{\boldsymbol{v}}^*$ can be defined in the following way for a large volume V

$$\overline{\boldsymbol{v}}^* = \frac{1}{\epsilon(V_{\mathrm{o}} + V_{\mathrm{w}})} \left(\int_{V_{\mathrm{o}}} \boldsymbol{v}_{\mathrm{o}}(t) \mathrm{d}^3 r + \int_{V_{\mathrm{w}}} \boldsymbol{v}_{\mathrm{w}}(t) \mathrm{d}^3 \boldsymbol{r} \right) = \frac{\overline{\boldsymbol{v}}_{\mathrm{o}} + \overline{\boldsymbol{v}}_{\mathrm{w}}}{\epsilon} \tag{17}$$

where V_{o} and V_{w} are the portions of the volume V occupied by oil and water, respectively.

Hence, the random walk technique has been chosen in order to determine these macroscopic quantities. This is not by any means a simple problem and the following difficulties were to be solved

(i) the problem of different diffusion coefficients in each phase,
(ii) the moving interfaces,
(iii) the definition of the velocity field in the ILB code.

These difficulties have been overcome and a program which works satisfactorily well was finally issued and will be presented in Section 2.3.4.

Let us end this introductory section by some notations. Phase 1 will correspond to oil, and phase 2 to water.

2.3.3. Random walks in multiphase flow

The transport by convection and diffusion of the particles suspended in two phase flow can be simulated by random walks. In this method, the trajectories of numerous tracers are followed individually. At time zero, a large number N_p of particles is released in the pore space. In order to speed up statistical convergence, the particles are released with a probability density proportional to the equilibrium concentration C_α^{eq} in the phase α. At each time step, the velocity field and the phase configuration are determined by the ILB method. Then during this time step of duration δt_α, the position $\boldsymbol{r}_i$ of the ith particle is incremented during the time step δt_α by $\boldsymbol{\delta}_{i\alpha}$

$$\boldsymbol{\delta}_{i\alpha} = \boldsymbol{v}(\boldsymbol{r}_i)\,\delta t_\alpha + \boldsymbol{\delta}_{d\alpha} \tag{18}$$

which is the sum of two terms. The term $\boldsymbol{v}(\boldsymbol{r}_i)\,\delta t_\alpha$ in Eq. (18) corresponds to the convective displacement of the particle in the phase $\alpha \cdot \boldsymbol{\delta}_{d\alpha}$ is a random displacement due to molecular diffusion. Its modulus δ_α is related to the diffusion coefficient D_α by

$$D_\alpha = \frac{\delta_\alpha^2}{6\delta t_\alpha} \tag{19}$$

The direction of the jump $\boldsymbol{\delta}_{d\alpha}$ is chosen at random with a random number generator.

It can be shown that the probability that a particle hits an interface during a single random displacement is proportional to the length of the displacement δ_i. Hence, the time rate of particles hitting an interface is proportional to $\delta_i/\delta t_i$. According to Eq. (1), the time rate of particles on the oil side is equal to K times the one of the water side and one obtains the following condition

$$\frac{\delta_2}{\delta t_2} = K\frac{\delta_1}{\delta t_1} \tag{20}$$

Thus, the elementary diffusive displacement in the oil phase δ_1 is related to the water one δ_2 by

$$\delta_1 = \frac{D_1}{D_2} K \delta_2 \tag{21}$$

The relation between the two time steps is thus given by

$$\delta t_1 = \frac{D_1}{D_2} K^2 \delta t_2 \tag{22}$$

The same problem has been solved in different ways by Tomadakis and Sotirchos (1996) and Labolle et al. (1996).

In order to keep the elementary jump $\delta_{i\alpha}$ reasonably small, δt_α is adjusted so that δ_α is as large as possible for a given Péclet number; this speeds up the statistical convergence; the following condition is imposed

$$|\delta_{i\alpha}| \leqslant \delta_M \tag{23}$$

where δ_M is the magnitude of the maximum modulus of the elementary jumps $\delta \boldsymbol{r}_i$. This parameter is crucial. It was set to half of the size of the elementary cubes

$$\delta_M = a/2 \tag{24}$$

This value was found to yield the best compromise between accuracy and computational time.

The time step δt_1 (i.e., δt_2) is related to the maximum jump δ_M by

$$\begin{cases} \delta_M \geqslant v^1_{\max}\delta t_1 + \sqrt{6D_1\delta t_1} \\ \delta_M \geqslant v^2_{\max}\frac{D_2}{D_1}K^2\delta t_1 + \sqrt{6\frac{D_2^2}{D_1}K^2\delta t_1} \end{cases} \tag{25}$$

When a particle reaches an interface, it stops and the elapsed time to arrive at this interface is recorded. The remaining time is used in the subsequent step with the physical parameter of the new phase. So the following directed step is calculated with the velocity and the random diffusion displacement according to the diffusion coefficient of the new phase. This following step may point into the new or old phase; if it points in the old phase, the particle does not leave the interface and the procedure is resumed until the particle stays in the chosen phase.

2.3.4. General organisation of the code

In order to summarize the previous developments, the code has been schematized in Fig. 1. All the calculations are done in the ILB units (cf. Ginzbourg and Adler (1995) for details); for instance, the unit length is equal to the size a of the elementary cubes and the unit time is the elementary time step of the ILB code.

First, input quantities are read such as the geometry of the medium, the physical constants and the dimensionless parameters.

An important quantity is the water saturation S_w which is kept constant for a given run. Since the phase configuration is a priori unknown, the ILB code starts from a given initial configuration which is usually made of two successive slices of oil and water as displayed in Fig. 9a. An overall pressure gradient $\overline{\nabla p}$ is imposed on both fluids.

Because of the spatially periodic boundary conditions, the fluids never leave the unit cell and the saturation is constant. It is important to note that one cannot speak in our simulations of drainage or imbibition conditions.

The ILB code is run without any dispersion until stationary conditions are reached. Note that the phase configuration will always keep changing with time. This point will be illustrated in Section 4.2.

Then the random walks are started. In order to be as close as possible to equilibrium, the particles are initially distributed at random in each phase, but the proportions indicated by the partition coefficient 1 are fulfilled. At each time step, each particle is moved according to Eq. (18) where the velocity field is provided by the ILB code. The ILB code is used again to determine a new phase configuration and a new velocity field.

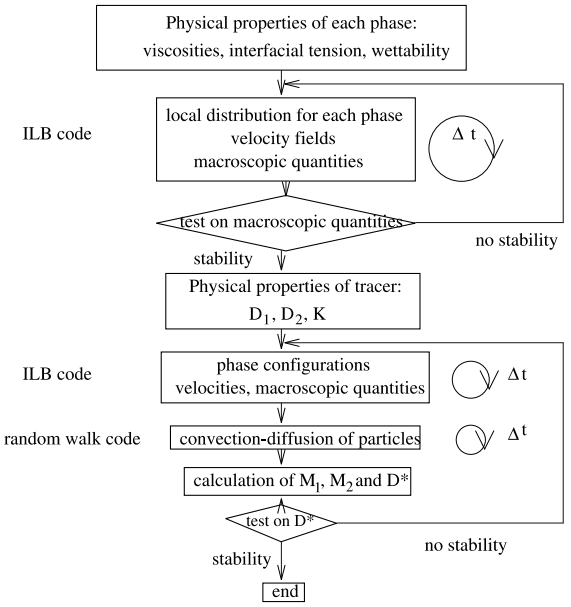

Fig. 1. General organization of the code.

Every several steps, the macroscopic quantities which characterize dispersion, namely the two first moments are computed. It is important to not that a stationary configuration would be a rough approximation of what is actually going on.

Finally, the code is stopped when the dispersion tensor has reached a stationary value.

3. Poiseuille flow: analytical

Poiseuille flow is an idealized situation where flow is one-dimensional with no slip boundary conditions at the walls. This elementary flow is often used as it is the only one for which an analytical solution to the Navier–Stokes equation can be obtained. In this study, the theoretical results obtained for Poiseuille flow will be compared with actual numerical data. It also gives us the opportunity of using the technique of the ***B***-equation.

3.1. Single phase Poiseuille flow

Consider two parallel at plates where flow is parallel to the x-axis; the y-axis is perpendicular to the plates as shown in Fig. 2a. When the pressure gradient is parallel to the x-axis, the Navier–Stokes equation reduces to its most basic form

$$\mu \frac{\mathrm{d}^2 u}{\mathrm{d}y^2} = \frac{\mathrm{d}p}{\mathrm{d}x} \tag{26}$$

whose solution is

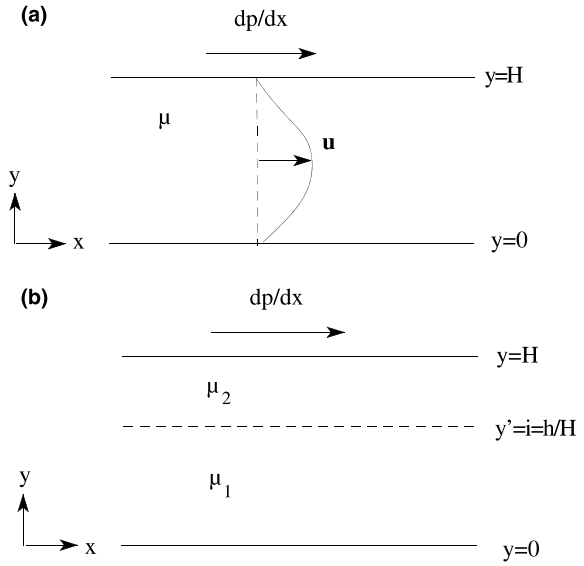

Fig. 2. Poiseuille flow for one (a) and two (b) phases between two planes.

$$u = \frac{1}{\mu}\frac{\mathrm{d}p}{\mathrm{d}x} y(H - y) \tag{27}$$

where $\mathrm{d}p/\mathrm{d}x$ is a given constant.

The dispersion tensor can be determined by using the method of the $\boldsymbol{B}$-equation due to Brenner (1980). The field $\boldsymbol{B}$ can be shown to be a solution of a vectorial convection–diffusion equation

$$\begin{cases} D \cdot \nabla^2 \boldsymbol{B} - \nabla \cdot (\boldsymbol{v}\boldsymbol{B}) = \overline{\boldsymbol{v}}_{\mathrm{c}}^{*} \\ n \cdot \nabla \boldsymbol{B} = 0 \quad \text{on the wall} \\ [\boldsymbol{B}] = -[\boldsymbol{r}] \\ [\nabla \boldsymbol{B}] = 0 \end{cases} \tag{28}$$

The dispersion tensor $\boldsymbol{D}^{*}$ can be expressed as

$$\boldsymbol{D}^{*} = \frac{D}{\tau_f} \int_{\tau_f} \nabla \boldsymbol{D}^{*\dagger} \cdot \nabla \boldsymbol{B}\, \mathrm{d}^3 \boldsymbol{r} \tag{29}$$

where τ_f is the volume of the unit cell.

As Poiseuille flow corresponds to a one dimensional problem, the previous partial differential equation reduces to a quadrature. $\boldsymbol{B}$ is reduced to its longitudinal component B_x and D_{xx}^{*} is recalled to be

$$D_{xx}^{*} = D\left(1 + \frac{Pe^2}{210}\right) \tag{30}$$

where Pe is given by Eq. (16) with $l = H$.

3.2. Two-phase Poiseuille flow by the **B**-equation

The physical situation for two phase Poiseuille flow is represented in Fig. 2b. Similar to the case of a single phase, the Stokes equation reduces to a one dimensional problem. y' is the vertical reduced coordinate

$$y' = \frac{y}{H} \tag{31}$$

The interface is located at $y' = 1 - S_w$. The two phases are denoted by the indices 1 and 2, or o and w, respectively. The velocities of both phases can be written as

$$\frac{v_1}{v_0} = 6y'(1 - y' + A)\frac{\mu_2}{\mu_1} \tag{32a}$$

$$\frac{v_2}{v_0} = 6(y' - A)(1 - y') \tag{32b}$$

where v_0 (which is the overall interstitial velocity defined by Eq. (17)) and A are given by

$$v_0 = \frac{H^2}{12}\frac{1}{\mu_2}\frac{\mathrm{d}p}{\mathrm{d}x} \tag{32c}$$

$$A = \frac{S_w(1 - S_w)(\mu_1 - \mu_2)}{\mu_2 + S_w(\mu_1 - \mu_2)} \tag{32d}$$

Thus, the average velocities of both phases are given by

$$\frac{\overline{v}_1}{v_0} = \frac{\mu_2}{\mu_1}(1 - S_w)^2[3(A + 1) - 2(1 - S_w)] \tag{33a}$$

$$\frac{\overline{v}_2}{v_0} = S_w^2(3 - 3A - 2S_w) \tag{33b}$$

Note that in this situation, there is no need to distinguish between interstitial and seepage velocities since one is interested by a single channel and the porosity is equal to 1, so to speak.

In a two-phase Poiseuille flow where the interface does not change position, the **B**-field method can be easily extended. The right-hand side of Eq. (28) must be generalized to the interstitial velocity $\overline{\boldsymbol{v}}_c^*$ of the solute with a partition coefficient K

$$\overline{\boldsymbol{v}}_c^* = \frac{K\overline{\boldsymbol{v}}^o + \overline{\boldsymbol{v}}^w}{K(1 - S_w) + S_w} \tag{34}$$

Moreover, the **B**-fields in the oil and water phase satisfy the same equation as before, but with additional conditions at the interface whose unit normal vector is $\boldsymbol{n}$

$$\begin{cases} D_k \cdot \nabla^2 \boldsymbol{B}_k - \nabla \cdot (\boldsymbol{v}_k \boldsymbol{B}_k) = \overline{\boldsymbol{v}}_c^*, \quad k = o, w \\ \boldsymbol{n} \cdot \nabla \boldsymbol{B}_k = 0 \quad \text{on the wall} \\ \boldsymbol{B}_o = \boldsymbol{B}_w, \quad D_o \boldsymbol{n} \cdot \nabla \boldsymbol{B}_o = D_w \boldsymbol{n} \cdot \nabla \boldsymbol{B}_w \quad \text{at the interface} \\ [\boldsymbol{B}] = -[\boldsymbol{r}] \\ [\nabla \boldsymbol{B}] = 0 \end{cases} \tag{35}$$

Because of the translational symmetry of the plane Poiseuille flow, the ***B***-equation (35) implies

$$\frac{D_1}{H^2}\frac{\mathrm{d}\breve{B}_{1x}}{\mathrm{d}y'} = \overline{v}_c^* y' + v_0\frac{\mu_2}{\mu_1}y'^2[2y' - 3(1+A)] \tag{36a}$$

$$\frac{D_2}{H^2}\frac{\mathrm{d}\breve{B}_{1x}}{\mathrm{d}y'} = \overline{v}_c^* y' + v_0 y'^2[2y' - 3(1+A)] + 6v_0 A y' + v_0(1-3A) - \overline{v}_c^* \tag{36b}$$

where $\breve{B}_{Kx}$ is the spatially periodic part of B_{Kx}

$$\breve{B}_{Kx} = B_{Kx} + x \tag{36c}$$

Consequently, the dispersion tensor (29) can again be defined in terms of $\breve{B}_x$, the spatially periodic component of the ***B***-field along the x-axis. The modification of Eq. (30) to incorporate two phases yields

$$[K(1-S_w)+S_w]D_{xx}^* = KD_1(1-S_w) + D_2 S_w + \frac{H^2}{D_1}K\int_0^{1-S_w}\left(\frac{D_1}{H^2}\frac{\mathrm{d}\breve{B}_{1x}}{\mathrm{d}y'}\right)^2\mathrm{d}y' + \frac{H^2}{D_2}\int_{1-S_w}^{1}\left(\frac{D_2}{H^2}\frac{\mathrm{d}\breve{B}_{1x}}{\mathrm{d}y'}\right)^2\mathrm{d}y' \tag{37}$$

where D_1 and D_2 are the diffusion coefficients in the two phases.

These cumbersome quadratures can be performed analytically. If we define an equivalent diffusion coefficient $\overline{D}$ by

$$\overline{D} = \frac{K(1-S_w)D_o + S_w D_w}{K(1-S_w)+S_w} \tag{38}$$

and an overall Péclet number $\overline{Pe}$ by

$$\overline{Pe} = \frac{\overline{v}_c^* H}{D}, \tag{39}$$

the macroscopic diffusion coefficient D_{xx}^* can be expressed under the same general form as single phase flow in a plane channel

$$D_{xx}^* = \overline{D}\left[1 + \frac{\overline{Pe}^2}{210}F_d\left(\frac{\mu_w}{\mu_o}, \frac{D_o}{D_w}, S_w, K\right)\right] \tag{40}$$

This expression is interesting in the sense that it separates the effect of the flow strength corresponding to the Péclet number and the influence of the other dimensionless parameters. Because of this separation, it was found useful to use $\overline{D}$ to normalize the macroscopic diffusion coefficient D^*. The full expression of F_d is given in Appendix A. Note that the viscosity and the diffusion coefficients have been treated in some of the following examples as independent parameters and that no use has been done of the Einstein relationship which relates the diffusion coefficient to viscosity.

Some systematic applications have been made of these analytical formulae in order to illustrate them. Numerical results corresponding to these analytical expressions are represented in Fig. 3.

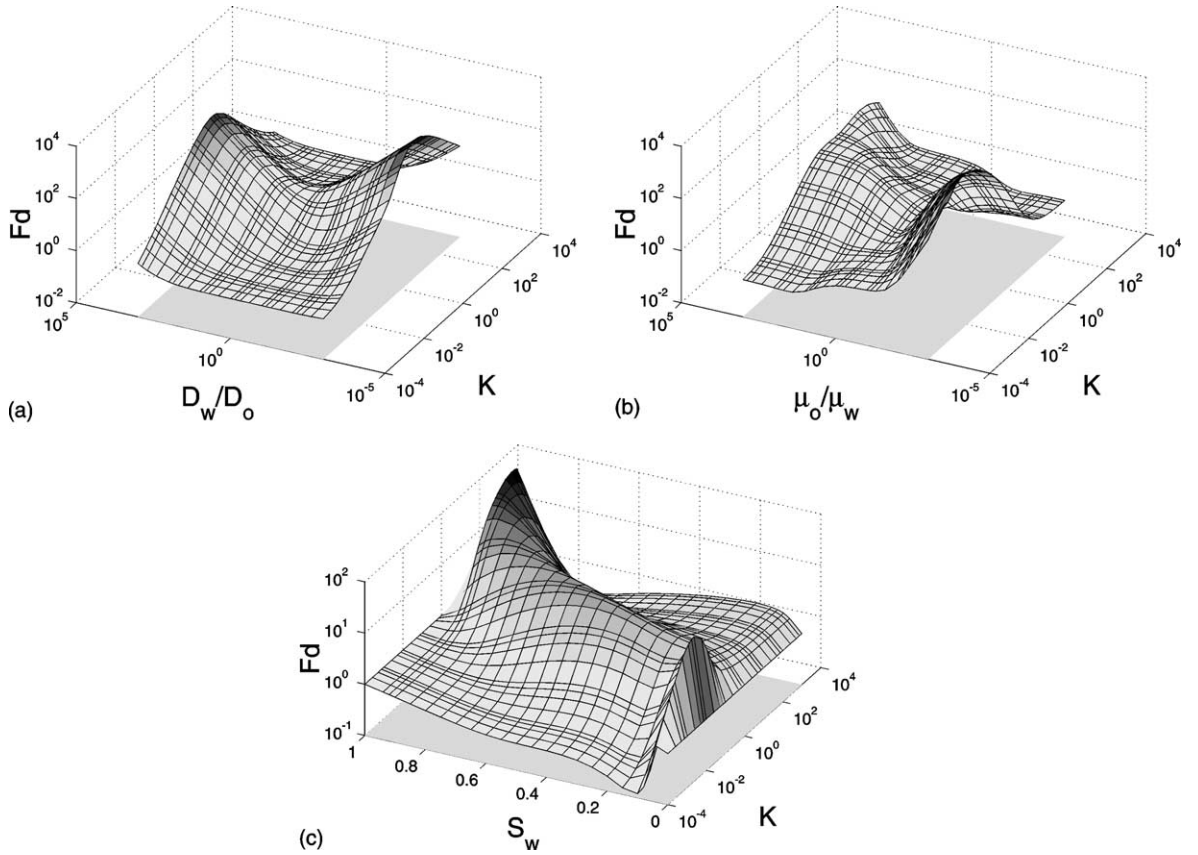

Fig. 3. Analytical variations of $F_d = (D^*_{xx}/\overline{D} - 1)210/\overline{Pe}^2$ with S_w, μ_o/μ_w, D_w/D_o and K; plane Poiseuille flow—in (a) $S_w = 0.5$ and $\mu_o/\mu_w = 10$, (b) $S_w = 0.5$ and $D_w/D_o = 10$, (c) $\mu_o/\mu_w = 10$ and $D_w/D_o = 10$.

This figure gives an overall view of the variations which are interesting since they are not monotonous. Note that for some values of the parameters, F_d tends towards one.

3.3. Two-phase Poiseuille flow by random walks

The numerical code has been first used in Poiseuille flow in order to check the random walk algorithm.

The general conditions are $H = 10a$, $S_w = 50\%$ and ($N_{cx} = 12$, $N_{cy} = 4$, $N_{cz} = 1$).

First, it was found important to check the influence of the partition coefficient in a motion less fluid. Such situations are displayed in Fig. 4. Initially, all the particles are put in fluid 2; they undergo diffusion and after some time, it is seen that the resulting partition coefficient is very close to its theoretical value. Of course, statistical fluctuations remain and they are expected to be of the order of $1/\sqrt{N}$, where N is the number of particles. Since N is equal to 1000, it is seen that the fluctuations are in agreement with this order of magnitude.

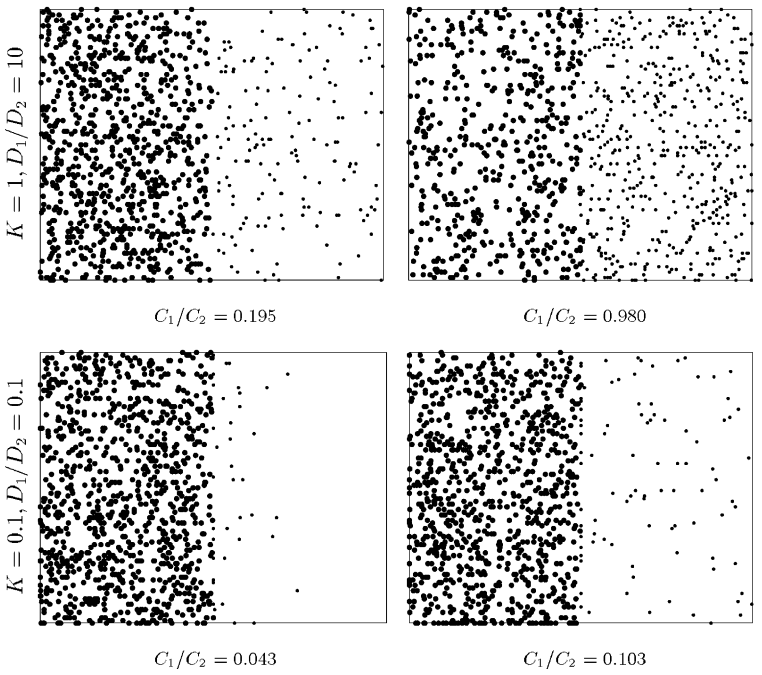

Fig. 4. Brownian motion of particles in a motionless two-phase fluid. The particles are initially put in fluid 2 located in the half-left of each figure. The particles located in fluid 2 are represented as bold dots. Each line corresponds to a given partition coefficient and a given ratio of the diffusion coefficients; the left and right columns correspond to a transient state and to equilibrium, respectively.

Then, dispersion was studied in two-phase Poiseuille flows for a saturation equal to 0.5 and for various values of the partition coefficient, of the ratios of the diffusion coefficients and of the viscosities

$$\begin{aligned}
&\frac{D_w}{D_o} = 0.1, 1, 10 \quad \text{for } K = 0.1, \qquad \frac{\mu_w}{\mu_o} = 0.1, \quad Pe = 100 \\
&\frac{D_w}{D_o} = 0.1, 1, 10 \quad \text{for } K = 1, \qquad \frac{\mu_w}{\mu_o} = 0.1, \quad Pe = 100 \\
&\frac{D_w}{D_o} = 0.1, 1, 10 \quad \text{for } K = 1, \qquad \frac{\mu_w}{\mu_o} = 1, \quad Pe = 100
\end{aligned} \tag{41}$$

The instantaneous positions of the particles are displayed in Fig. 5. The general trends are as expected, namely the clouds of particles are carried by the fluids and simultaneously their size increases. It is particularly interesting to note that even when the viscosity ratio of the two phases is equal to 10, the two clouds of particles in each phase remain very close one to another. This means that the transversal exchanges between the two fluids act against the separation of the solute in each phase, despite the possible large velocity difference. It is interesting to note that this behavior is somehow contrary to what was expected on an intuitive basis.

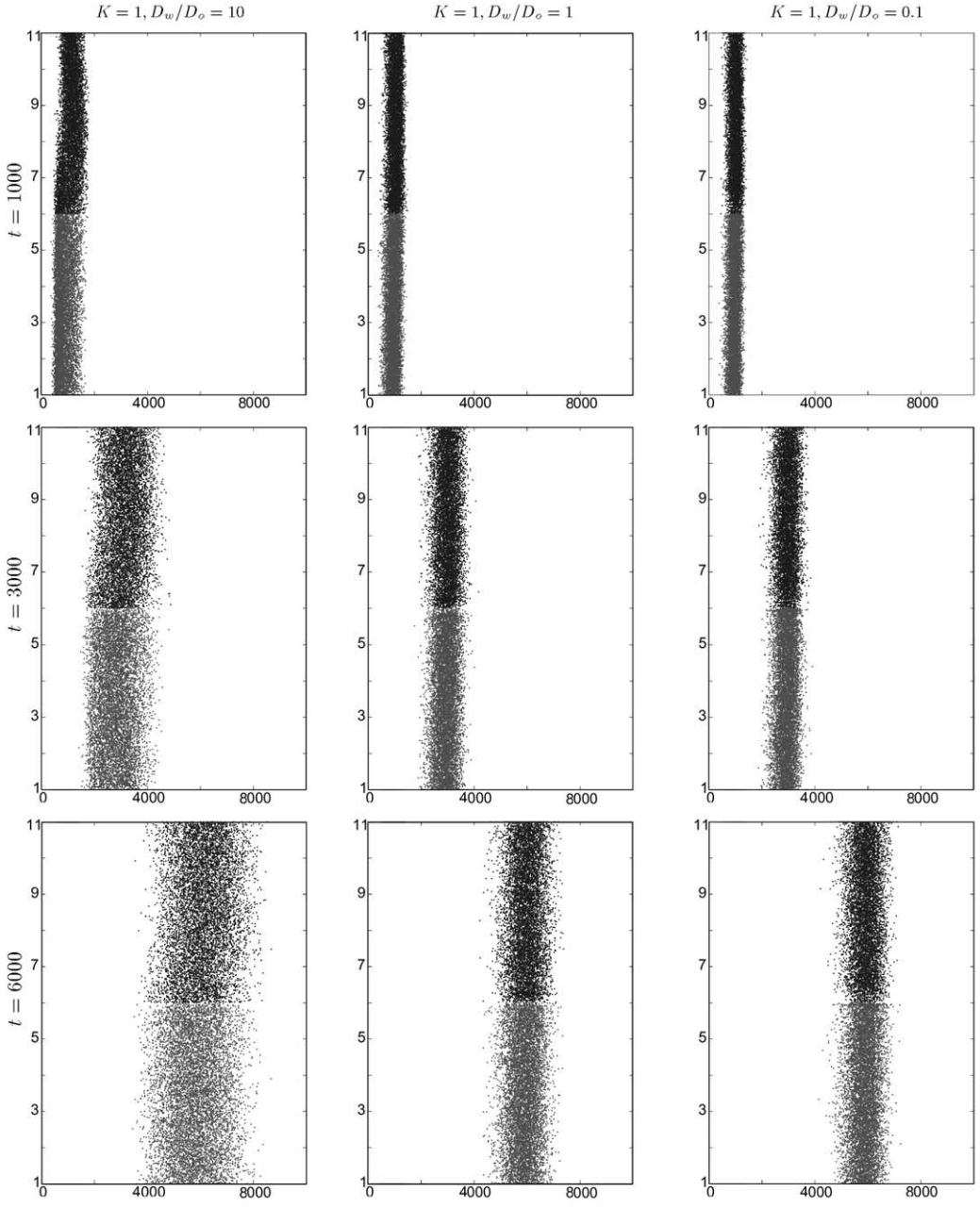

Fig. 5. Time evolution of Brownian particles dispersing in a two phase oil/water mixture in a two-phase Poiseuille flow. The particles located in the oil phase are represented in gray. Data are for: $S_w = 50\%$, $\mu_w/\mu_o = 0.1$ and $Pe = 100$.

The positions of the particles can be used to derive the dispersion coefficient D^*_{xx} according to Eq. (13b). Some results are given in Fig. 6. After an initial period where transient values are

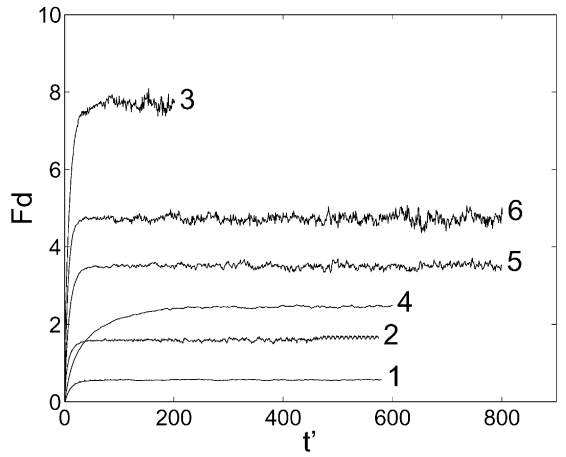

Fig. 6. Time evolution of the dispersion coefficient $((D^*_{xx}/\overline{D} - 1)210/Pe^2) \equiv F_d$ for a plane Poiseuille flow of a two phase oil/water mixture. The following coefficients were kept constant: $S_w = 50\%$, $Pe = 100$ and $\mu_w/\mu_o = 0.1$. Data are for: 1 ($K = 0.1$ and $D_w/D_o = 10$); 2 ($K = 0.1$ and $D_w/D_o = 1$); 3 ($K = 0.1$ and $D_w/D_o = 0.1$); 4 ($K = 1$ and $D_w/D_o = 10$); 5 ($K = 1$ and $D_w/D_o = 1$); 6 ($K = 1$ and $D_w/D_o = 0.1$).

Table 1
Comparison between numerical and analytical dispersion coefficients in Poiseuille flow

D_w/D_o	K	Num.	Anal.	Error (%)
0.1	0.1	7.76	7.53	3
0.1	1	24.4	24.2	1
1	0.1	86	81.8	5
1	1	185	181.3	2
10	0.1	1747	1589	10
10	1	1378	1288	7

Data are for: $\mu_w/\mu_o = 0.1$ and $Pe = 10$.

obtained, the dispersion coefficient fluctuates around an average value; the fluctuations are roughly proportional to the value of the dispersion coefficient.

The numerical results are found in agreement with the analytical results as displayed in Table 1. Note that other results have been obtained when the two fluids have the same properties and behave as a single fluid. It is seen that the error is always smaller than 10%. To conclude, it appears that our code works satisfactorily.

4. Dispersion in reconstructed porous media

4.1. Range of studied parameters

Two series of images were provided to us by Saga and Statoil on which the reconstructed porous media were based. Let us briefly comment on this step.

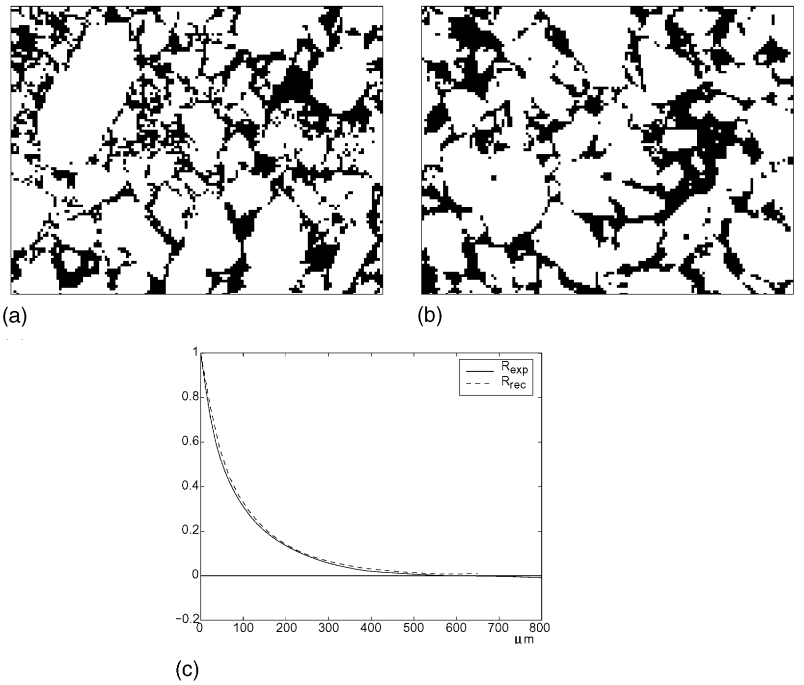

Fig. 7. Sample *sa*1865. The binary images *sa*1865*x*1*t* and *sa*1865*z*1*t* are displayed in (a) and (b); the image dimensions are 5.7×4.5 mm^2. (c) The correlation functions measured on the image is compared to the one measured on the reconstructed media; the lag is in microns.

The data set SAGA consisted of nine binary images *sa*1865. Five images were taken for each sample in both *x*- and *z*-directions, i.e., 10 images per sample, labeled x_1 to x_5 and z_1 to z_5. Two binary images are displayed in Fig. 7.

The data set STATOIL consisted of binary images from several samples, labeled *sb*, *sd* and *sf*. This core did not show any lamination, hence only thin sections in one direction were cut. Five images were taken for each sample, labeled 1–5. Two binary images are displayed in Fig. 8a.

Homogeneity and isotropy verifications were done according to our standard techniques (cf. Adler and Thovert, 1998) and some images were rejected.

The averages of the correlation functions over the retained images are given in Figs. 7c and 8c. The average properties used for the generation of the reconstructed samples are summarized in Table 2. The reconstructed samples are made of 48^3 or 64^3 elementary cubes of size a, entirely filled with either solid or void. The cube size a was set equal to twice the pixel size on the original images. $\mathcal{N} = 8$ or 10 samples were reconstructed in each case. The geometrical characteristics of the reconstructed samples (porosity ϵ, open porosity ϵ_0, and correlation length $\mathscr{L}$) are given in Table 2, in comparison with the experimental data. The correlation functions of the reconstructed media are compared to the experimental ones in Figs. 7c and 8c. The porosities and correlation lengths of the reconstructed samples are always very close to their experimental values. The correlation functions measured on the images and on the simulated materials are also in very good agreement. All the reconstructed samples percolate along the *x*-, *y*- and *z*-axes. The open and total

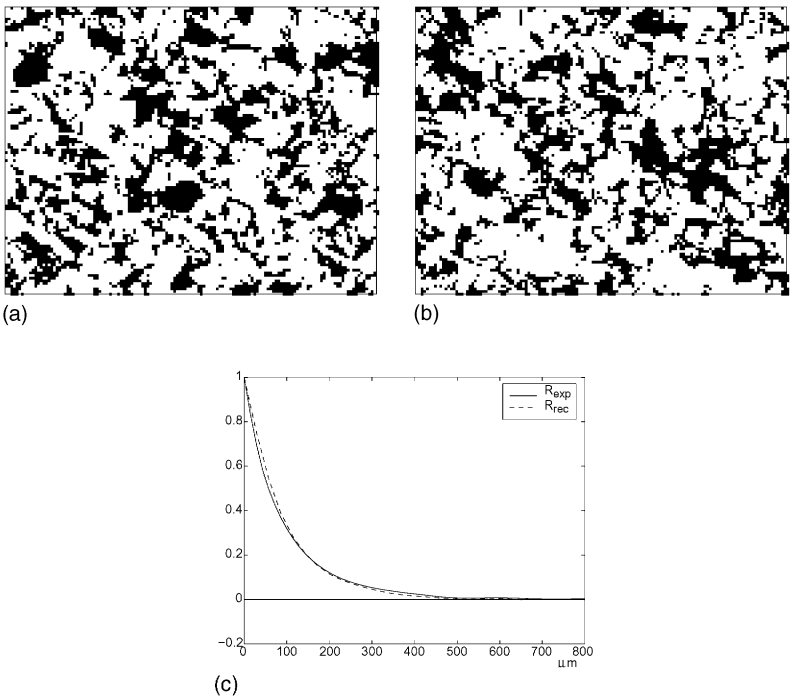

Fig. 8. Sample *sd*. The binary images *sd*1*t* and *sd*2*t* are displayed in (a) and (b); the image dimensions are 2.3×1.8 mm^2. (c) The correlation functions measured on the image is compared to the one measured on the reconstructed media; the lag is in microns.

Table 2
Geometrical parameters for the samples from experimental measurements and from numerical simulations

Image	Experimental		Simulation					
	ϵ_{exp}	$\mathscr{L}_{exp}$ (μm)	N_c	a	$\mathscr{N}$	$\bar{\epsilon}$	$\bar{\epsilon}_0$	$\mathscr{L}$ (μm)
*sa*1865	0.267	95.76	64	22.40	8	0.267 (0.09)	0.261 (0.10)	98.291
sd	0.371	32.1	48	8.96	10	0.365 (0.16)	0.363 (0.16)	34.0
			64	8.96	10	0.371 (0.06)	0.369 (0.06)	34.0

Numbers in parenthesis are standard deviations.

porosities are very similar. The closed porosity $\epsilon_c = \epsilon - \epsilon_o$ is smaller than 0.008 for SAGA and than 0.005 for STATOIL.

Let us now present the set of calculations which was started in this study. In order to limit the number of computations, a few physical parameters were kept fixed. These are the following (given in lattice units)

1. The viscosities of the two fluids are $\nu^o = 1.5$, $\nu^w = 0.15$.
2. The interfacial tension was chosen to be $\sigma = 5.5 \times 10^{-3}$.
3. The ratio between the diffusion coefficients is equal to $D_o/D_w = 0.1$.

Table 3
Set of physical parameters for numerical calculations in reconstructed media

	Saturation	20%	40%	50%	60%
$Pe = 0.1$	$K = 1$	×	×	×	×
	$K = 10$	×	×	×	×
$Pe = 1$	$K = 0.1$	○	○	○	○
	$K = 1$	×	×	×	×
	$K = 10$	×	×	×	×
$Pe = 10$	$K = 0.1$	× ○	× ○	× ○	× ○
	$K = 1$	×	×	×	×
	$K = 10$	×	×	×	×
$Pe = 100$	$K = 0.1$	× ○	× ○	× ○	× ○
	$K = 1$	×	×	×	×
	$K = 10$	×	×	×	×

Data are: (○) for *Statoil sd* and (×) for *Saga* 1865.

4. The pressure gradient is set along the x-axis. One value is used $|\nabla p| = 2 \times 10^{-3}$. It can be varied provided that it is not too large.
5. Water (phase 2) is supposed to preferentially wet the walls as indicated below. This parameter can be varied at will.
6. Periodic boundary conditions are used at the ends of the unit cell; this is a convenient and standard way to proceed.
7. The computations have been started for two reconstructed samples denoted by *Saga* 1865 and *Statoil sd*. Initial computations have been limited to these two samples since the algorithms are quite long and since the final number of independent parameters is quite large. The porosities of these two samples are equal to 0.27 and 0.37. These reconstructed samples are selected by checking the porosity and the correlation function. These numerical samples are relatively small since they contain 40 elementary cubes along each direction. The cube size was set equal to twice the pixel size. Hence, the physical sample size is $(0.36\ \text{mm})^3$ for *Statoil sd* and $(0.90\ \text{mm})^3$ for *Saga* 1865.

Then, three parameters were sytematically varied as displayed in Table 3, namely the partition coefficient which takes three values, the saturation and the Péclet number. Note that constant values of this last number were obtained by varying each diffusion coefficient, while keeping a given ratio between the phases.

4.2. Porous media and general transport properties

When a two-phase mixture is flowing through a porous medium, the geometry of the interface between the two fluids changes constantly. This situation is illustrated in Fig. 9. As stated in Section 2.3.4, the two fluids are initially placed in two slices perpendicular to the average pressure gradient. Spatially periodic boundary conditions are used and the fluid which goes out of the cell through one side, goes back into it through the opposite side. In order to have a better view on the liquid phases, the solid phase has been removed. After some time, i.e., 2×10^5 iterations, the

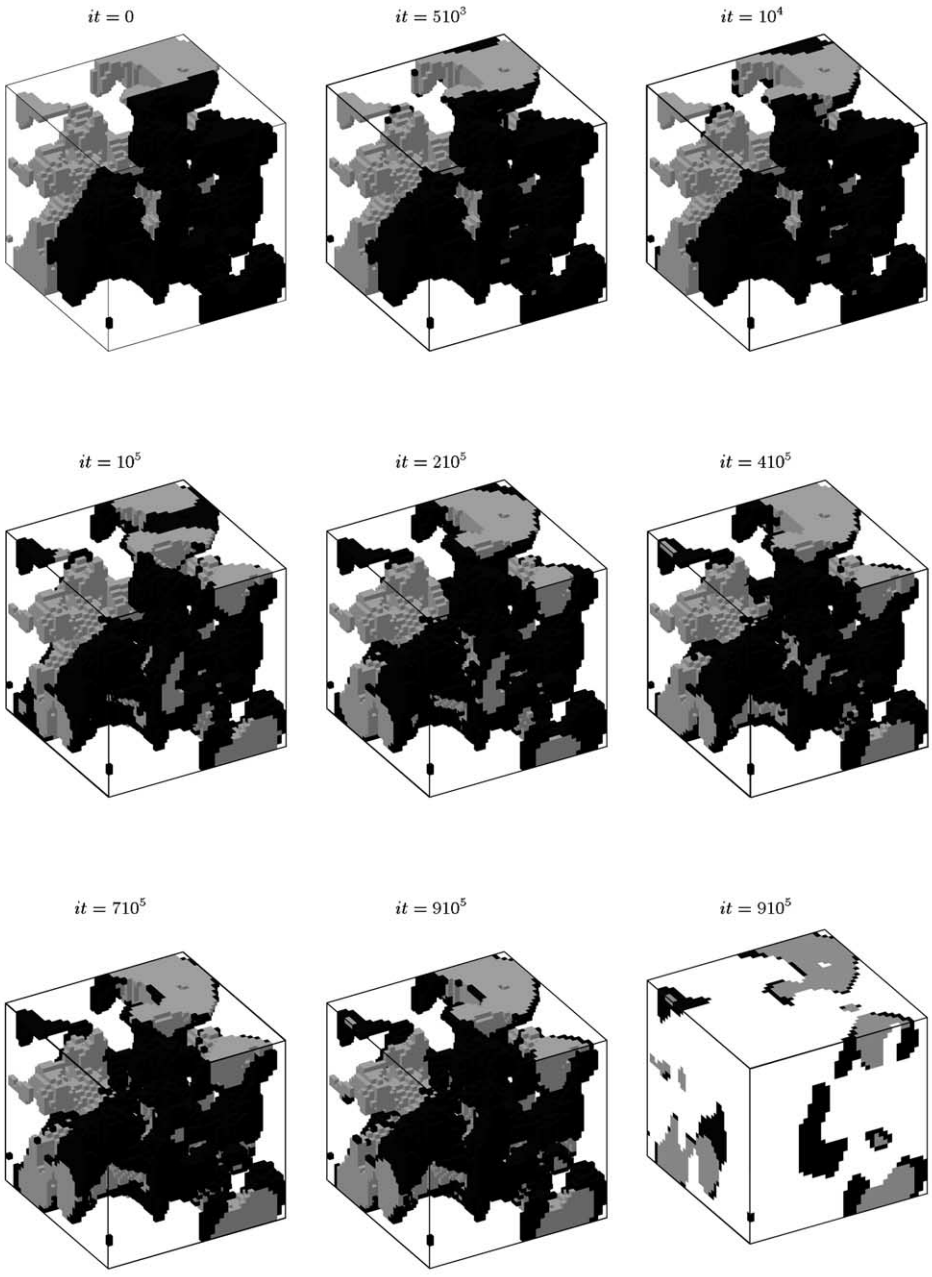

Fig. 9. Three-dimensional illustration of the phase distributions for various times in sample *Saga* 1865. $S_w = 50\%$. The pressure gradient is along the x-direction and the fluids flow from the back to the front. Color conventions are: oil (gray), water (black); the solid is omitted in all the pictures, except in the last one where it is white, but opaque.

general shapes of the domains occupied by the two phases are roughly constant; in particular a sort of large channel has been created in the middle of the sample; however, when some attention

is paid to details, it is seen that these shapes are constantly changing even after long periods of time.

In the last picture of Fig. 9, the solid phase has been represented again after a large number of iterations. The influence of the wettability is clearly seen in these pictures since water is mostly located at the walls. Other computations for different samples yield the reverse situation when oil is the wetting phase.

Macroscopic quantities such as the permeabilities K_w and K_o and such as the capillary pressure $p_c = p_o - p_w$ can be derived by integrating the local velocity and pressure fields over the unit cell. Instantaneous quantities can be obtained, but also time-averaged ones; the latter actually correspond to what is needed in the large scale simulators. Results are given in Fig. 10 for some permeabilities for the two samples and for the various saturations which were studied. This set of results can be briefly commented as follows. The arbitrary initial distribution generally implies a fast decrease of the macroscopic quantities during the first iterations; in a few opportunities, one has a slight increase (see Fig. 10d, $S_w = 40\%$ for instance). The instantaneous fluxes are seen to be random in character with time. However, when the permeabilities are time-averaged, they tend towards constant values after a large number of iterations which depends on the sample and on water saturation. Sometimes for $S_w = 20\%$, water permeability does not seem to converge; this impression is due to the vertical logarithmic scale; K_w is indeed very small, if not equal to zero for practical purposes.

The capillary numbers defined by Eq. (8) are relatively high for this set of numerical experiments. In the Saga set of calculations, C_o is of the order of 10^{-3}, while C_w ranges from 10^{-3} to 10^{-4} (except for S_w where it is equal to 10^{-7}). In the Statoil set, S_o is about 10^{-2} and S_w ranges between 10^{-4} and 10^{-3}.

The permeabilities of the samples *Saga* 1865 and *Statoil sd* are presented in Table 4. Note that the permeabilities display expected trends with saturation variations. The fact that the oil relative permeability is larger than 1 is mostly due to the large value of the capillary numbers; it is also due to the large viscosity ratio and to the fact that water is the wetting phase; a ratio closer to 1 would yield a value of K_{ro} smaller than 1 as shown by Békri et al. (in preparation). As noticed earlier, the saturations are imposed and do not depend on the capillary number; hence, the process is neither imbibition, nor drainage.

The effect of the size of the unit cell has not been systematically studied, but it was shown by Békri et al. (in preparation) that the influence of the size on permeability was not too important.

4.3. Dispersion

The definition (13b) was applied for finite times in order to obtain a dispersion tensor which is function of time

$$\boldsymbol{D}^*(t) = \frac{1}{2}\frac{\mathrm{d}\boldsymbol{M}_2}{\mathrm{d}t} \tag{42}$$

For sake of keeping simple notations, the dependence on time is often omitted in the following.

It might be useful to emphasize that dimensionless expressions of the dispersion tensor $\boldsymbol{D}^*/\overline{D}$ a priori depend on many dimensionless parameters. The expression (40) obtained for Poiseuille flow can be easily generalized as

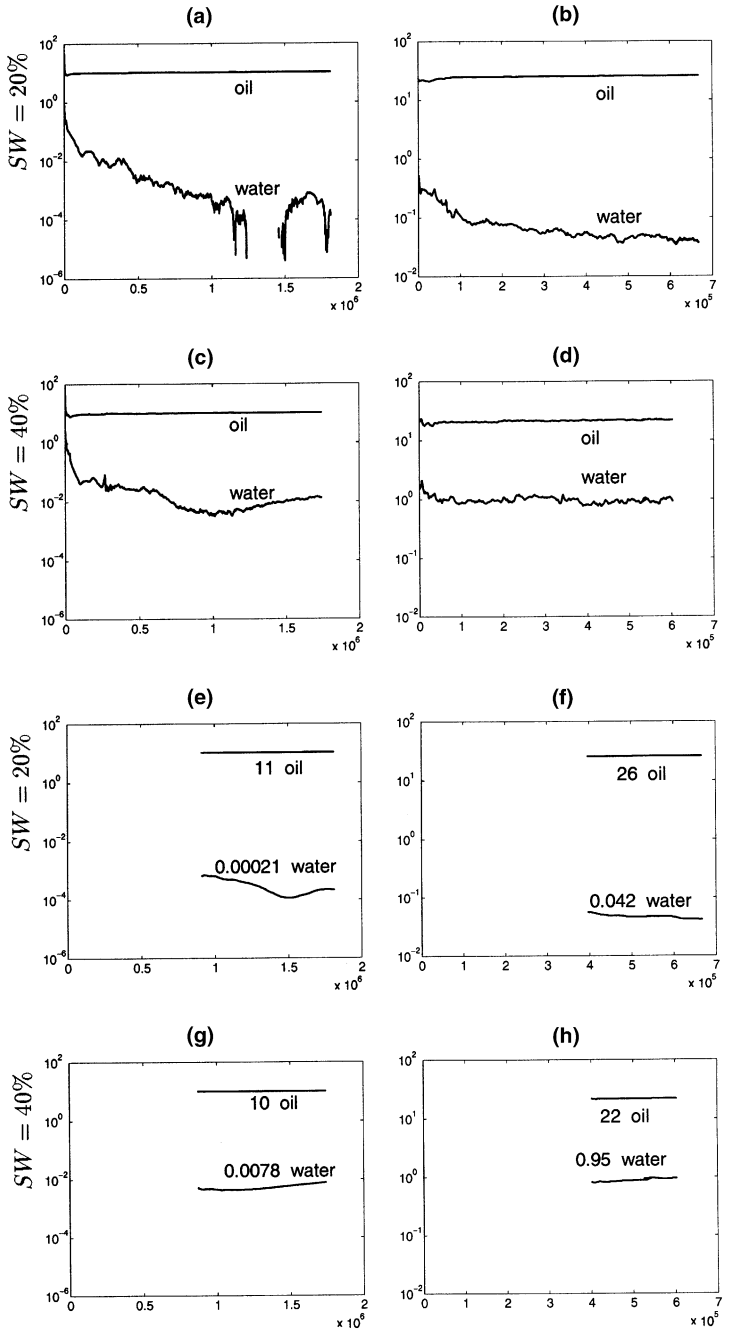

Fig. 10. Time evolution of the instantaneous (a)–(d) and time average (e)–(h) permeabilities K^{α} [*Darcy*] in the samples *Saga* 1865 (left column) and *Statoil sd* (right column). Data are for: water wets; $|\nabla p| = 2 \times 10^{-3}$; $S_w = 20\%$, 40%.

Table 4
Permeabilities K[*Darcy*] along the *x-axis* for *Saga* 1865 and *Statoil sd*

Sample		$S_w = 20\%$	$S_w = 40\%$	$S_w = 50\%$	$S_w = 60\%$	$S_w = 100\%$
Saga	K_o	11	10	9.7	6.7	3.2
	K_w	0.00021	0.0078	0.098	0.59	3.2
Statoil	K_o	26	22	18	15	11
	K_w	0.042	0.96	1.7	2.7	11

$$\frac{\boldsymbol{D}^*}{\overline{D}} = \frac{\boldsymbol{D}^*}{\overline{D}}\left[Pe, \frac{\mu_w}{\mu_o}, \frac{D_o}{D_w}, S_w, K, \mathscr{G}\right] \tag{43a}$$

where the Péclet number Pe for reconstructed media is defined as

$$Pe = \frac{\overline{v}^* \mathscr{L}}{\overline{D}} \tag{43b}$$

where $\mathscr{L}$ is the correlation length Eq. (5) and $\overline{D}$ the diffusion coefficient used in the Poiseuille formula (38). It was found useful to use this expression which is theoretically justified. Moreover, no phase is arbitrarily privileged by this choice and it takes into account the variations of S_w and K. For instance, one obtains the right limits when $S_w = 0$ or 1, and when $K = 0, \infty$.

Finally, the symbol $\mathscr{G}$ represents the geometry of the porous medium. Here, $\mathscr{G}$ corresponds to the porosity ϵ and the correlation function $R_Z(u)$. Like the other macroscopic properties such as the conductivity and permeability, $\boldsymbol{D}^*$ reflects at least partly the geometry of the medium.

The dispersion tensor is separated into its parallel and perpendicular components. With our present notations, the average pressure drop is directed along the x-axis; thus, this implies that the parallel component is denoted by D_x^* and the two perpendicular components by D_y^* and D_z^*. Figs. 11 and 12 represent some time evolutions of $\boldsymbol{D}^*$ along the xyz-axes in both samples. These figures are only a brief illustrative abstract of the large set of results that we obtained for all the parameters listed in Table 3.

Note that by dividing the dispersion tensor $\boldsymbol{D}^*$ by the Péclet number Pe, one obtains a relation which is almost linear. Hence, multiphase flows through porous media yield results very similar to single phase Poiseuille flow where D^*/Pe is a linear function of the Péclet number.

Generally speaking, it is seen for all the Péclet numbers that the transversal components are much smaller than the longitudinal one; this is a fact which is also true in single phase flow. It is interesting to note that D_y^* and D_z^* are of the same order of magnitude as they should since the samples are statistically isotropic.

Whatever the value of time and the location within the computing process, most of the fluctuations are probably due to the changes in the phase configurations. Since the unit cells are relatively small, the fluctuations are not sufficiently averaged.

Let us first discuss the time dependency of the results displayed in these two figures. Three regions can be distinguished for the sake of clarity. In the initial phase, the effect of the transient distribution of the phases is clearly seen; there is no general rule since sometimes the dispersion coefficient undergoes a sudden increase or a sudden decrease. It might be useful to recall that the solute has been distributed initially according to the partition coefficient; hence, the transient cannot be attributed to a redistribution of the solute. For large times, it is seen that some asymptotic values are hard to obtain, especially for the longitudinal component, for large Pe and

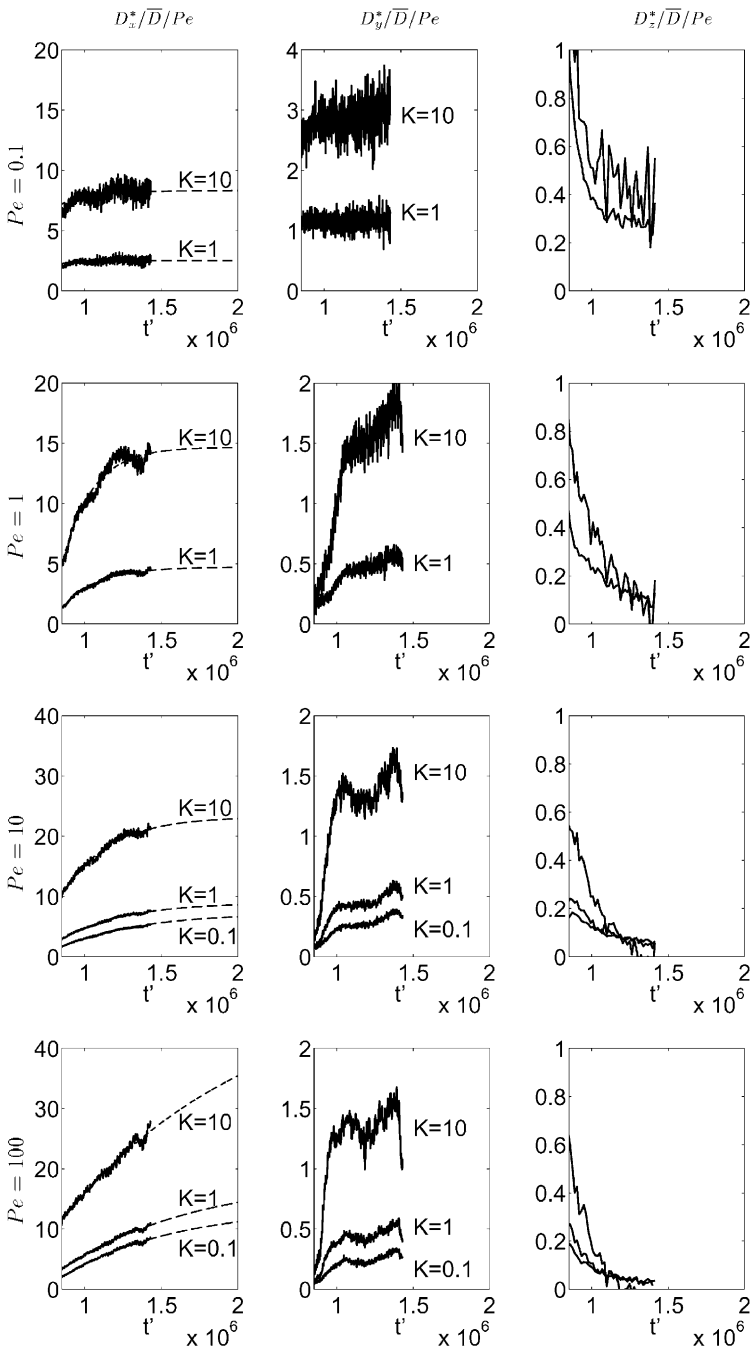

Fig. 11. Time evolution of dispersion coefficients normalized by $\overline{D}$ and Pe in the sample *Saga* 1865. Data are for $|\nabla p| = 2 \times 10^{-3}$, $S_w = 60\%$ and water phase wets the walls. The dotted line in the left row corresponds to Eq. (44).

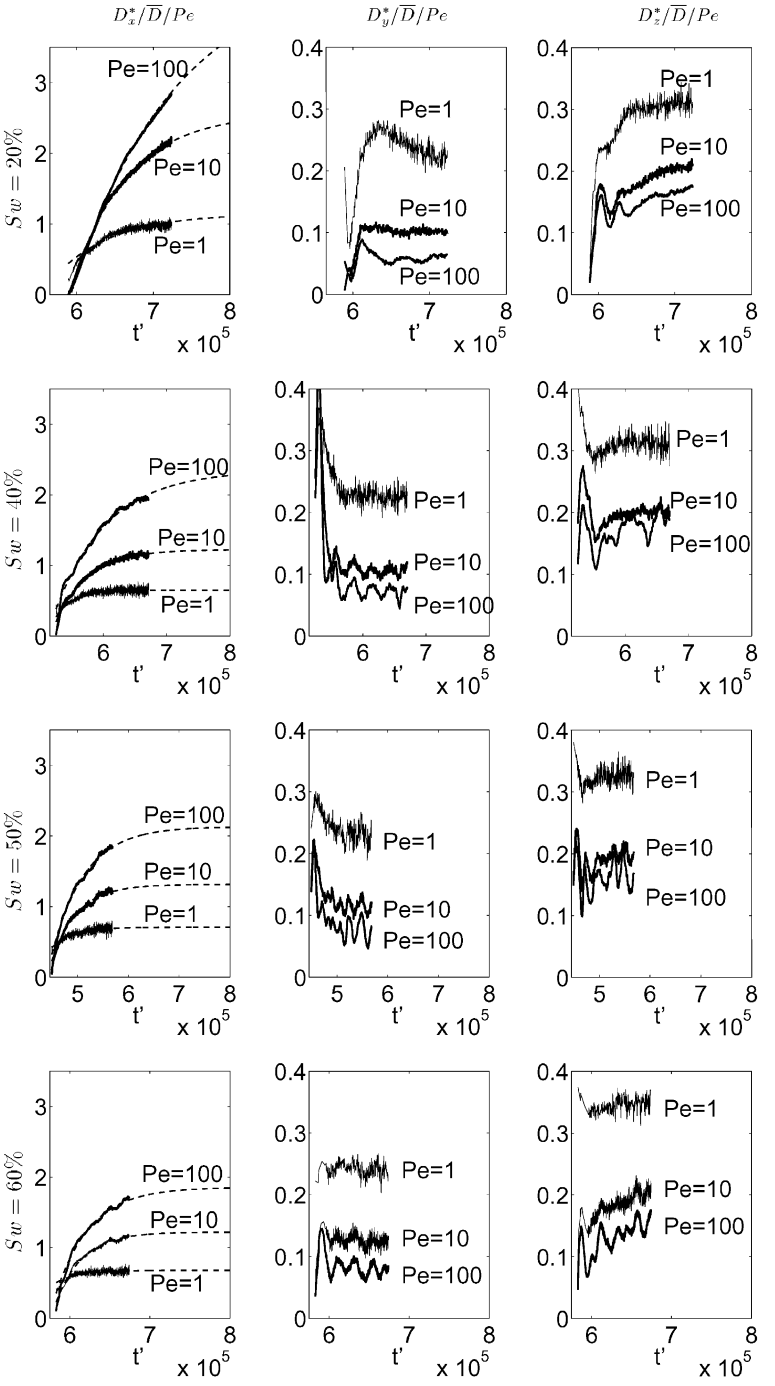

Fig. 12. Time evolution of dispersion coefficients normalized by $\overline{D}$ and Pe in the sample *Statoil sd.* Data are for $|\nabla p| = 2 \times 10^{-3}$, $K = 0.1$ and water phase wets the walls. The dotted line in the left row corresponds to Eq. (44).

for large values of the partition coefficient (i.e., when the solute is mostly in the oil phase). For intermediate times, some short time fluctuations are always added to the long term behaviour of the dispersion coefficients.

Let us now discuss qualitatively the influence of the other parameters. The role of the Péclet number is quite obvious; as in single phase flow, $\boldsymbol{D}^*$ is an increasing function of this parameter. The partition coefficient K has a similar in influence; however, it should be reminded that in our case, water is the wetting phase, and that it has been shown to remain confined close to the walls (cf. Fig. 9); a very different behaviour would probably be obtained in the opposite situation.

The last important parameter which has been systematically studied is S_w; it is interesting to note that in some cases, it may yield either an increase or a decrease of the dispersion tensor. This important feature will be fully documented in the next subsection.

Another crucial feature is the fact that the two samples have quite different behaviors; this might be due to the different phase distributions which are apparent in the samples.

4.4. Correlations

It is clear from the Figs. 11 and 12 that often the data along the x-axis are not fully converged yet in time. However, we know (see Brenner, 1980) that the asymptotic behavior of the second moment should be of the general form

$$D_x^*(t) = D_{x\infty}^*(1 - ke^{-t/T}) \tag{44}$$

This form was fit to the experimental data along the x-axis by using the Levenberg–Marquardt method as described by Press et al. (1992). It is seen in Figs. 11 and 12 that the proposed formula represents very well the time evolution of D_x^*.

The most complete analysis has been performed for the sample *Saga* 1865. Some values are missing which correspond to the cases where the computations have not been long enough to converge sufficiently well, a situation which occurs quite often for $Pe = 100$, especially when $S_w = 0.2$.

Then these asymptotic values are successfully analyzed as functions of Pe and S_w. The regressions as functions of Pe are performed first and they are illustrated in Fig. 13. The values of D_x^* based on the last calculated values by means of Eq. (42) have also been displayed in this figure for sake of completeness; this gives an estimate of the errors made in the determination of D_x^*; in most cases, the values are in quite good agreement and in the rest of this paper we shall only use the values based on Eq. (44). Generally speaking, the correlation by a power law is a good approximation to the results and a least-square fit of D_x^* was systematically performed.

The same work was done on the transversal coefficients D_y^* and D_z^*; some of them are displayed in Fig. 14. Note that it is useless to use the regression technique Eq. (44) in these cases since the asymptotic regime is always reached.

Again a power law appears to be adequate to fit the results. An interesting feature which arises from a comparison between the data is that the transversal coefficients do not depend on saturation. This dependence of the dispersion tensor as a power law of the Péclet number is not surprising since it is in this way that most data are analyzed in the literature (as reported by Adler et al. (1990) and by Sallès et al. (1993)).

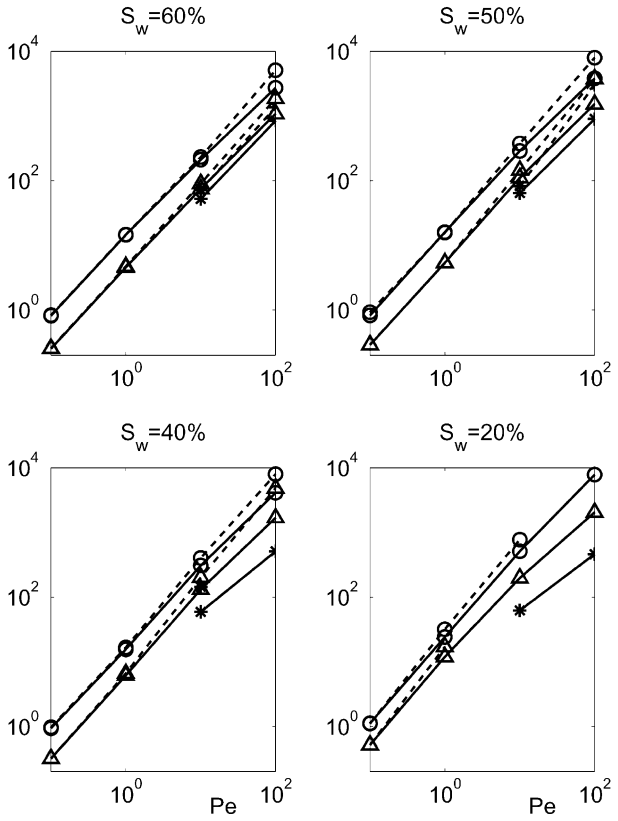

Fig. 13. Longitudinal dispersion coefficients (x-axis) normalized by $\overline{D}$ as functions of Péclet number in the sample *Saga* 1865. Conventions are: $K = 0.1$ (✻), $K = 1$ (△), $K = 10$ (○). The solid lines correspond to the last calculated values (42) and the broken lines to the least square fit (44).

Finally, D_x^* is represented as a function of saturation in Fig. 15, when the other parameters are kept fixed. Again a power law appears to represent the experimental results reasonably well; in all cases where the calculations are satisfactorily converged, it is a decreasing function of S_w; the exponent depends on the Péclet number and on the partition coefficient K. It should be emphasized that there is no theoretical justification behind this representation of dispersion as a power law of saturation. It can be simply taken as a convenient way of summarizing the results over the interval of saturations which were studied here.

When all the regressions are made, the data for the sample *Saga* 1865 can be summarized by two series of relations. The first one is based on Eq. (42) with an average over the last values

$$D_x^*/\overline{D} \approx 10 S_w^{-0.55} Pe^{1.24} \quad \text{for } K = 10 \tag{45a}$$

$$D_x^*/\overline{D} \approx 3 S_w^{-0.85} Pe^{1.27} \quad \text{for } K = 1 \tag{45b}$$

$$D_x^*/\overline{D} \approx 5 S_w^{-0.65} Pe^{1.21} \quad \text{for } K = 0.1 \tag{45c}$$

$$D_y^*/\overline{D} \approx Pe^{0.96} \quad \text{and} \quad D_z^*/\overline{D} \approx Pe^{0.60} \tag{45d}$$

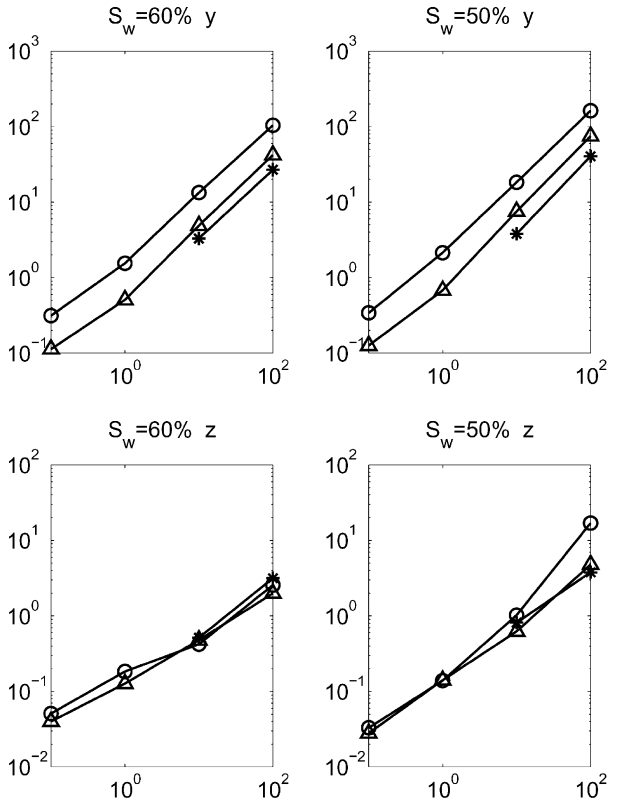

Fig. 14. Transversal dispersion coefficients (y- and z-axes) normalized by $\overline{D}$ as functions of Péclet number in the sample *Saga* 1865. Conventions are: $K = 0.1$ (✻), $K = 1$ (△), $K = 10$ (○). Data are based on the last calculated values (42).

The other relations are based on the least-square fit of Eq. (44)

$$D_x^*/\overline{D} \approx 12 S_w^{-0.75} Pe^{1.27} \quad \text{for } K = 10 \tag{46a}$$

$$D_x^*/\overline{D} \approx 3 S_w^{-1.0} Pe^{1.27} \quad \text{for } K = 1 \tag{46b}$$

$$D_x^*/\overline{D} \approx 5 S_w^{-0.45} Pe^{1.28} \quad \text{for } K = 0.1 \tag{46c}$$

As a general comment, these correlations should not be used out of the variable intervals where they were established. For instance, the fact that D^* diverges when S_w tends towards 0 should be taken with care, though it might not be without any physical justification as we shall see below.

First, the correlations obtained in one way or another are not very different in most cases; the transversal coefficients are always well converged and do not necessitate any extrapolation by Eq. (44). Moreover, the exponent of the Péclet number for the longitudinal component D_x^* does not depend on the partition coefficient; it is by the way quite close to the standard values in single phase flow (cf. for instance the references gathered in Adler (1992)); however, the coefficient in front of the law depends on K.

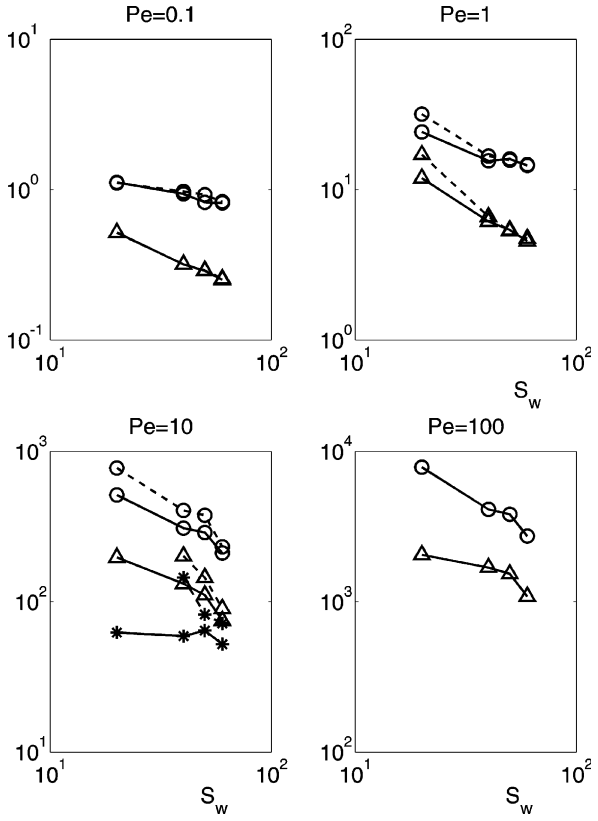

Fig. 15. Longitudinal dispersion coefficients (x-axis) normalized by $\overline{D}$ as functions of S_w in the sample *Saga* 1865. Conventions are: $K = 0.1$ (✻), $K = 1$ (△), $K = 10$ (○). The solid lines correspond to the last calculated values (42) and the broken lines to the least square fit (44).

An interesting feature is the dependence on S_w which is itself influenced by K. For small K, the solute is mostly in water which is close to the wall because of wettability. For large values of K, the opposite happens.

Let us focus our attention on the region at low saturation. On one hand, the numerical results indicate that D_x^* diverges; this might be qualitatively explained by the fact that when S_w tends towards 0, K_{rw} is almost zero which means that water is almost motionless and that it still contains particles; hence, dispersion increases when S_w goes to zero.

However, the experiments of Delshad et al. (1985) and of Salter and Mohanty (1982) show that as the wetting-phase saturation decreases, the dispersion coefficients first increase and reach a maximum and then decrease. This does not agree with our calculations; this effect might be due to the fact that the numerical tracer is always partitioning; hence, one expects different effects for $K = 0$ and ∞.

Finally, one could note that one does not expect a symmetrical situation when $S_w \to 1$ since according to Table 4, K_{ro} does not go to zero in this limit. This difference is due to the fact that water is the wetting phase.

The results relative to the transversal components present some more simple features since they depend neither on K, nor on S_w; the exponents are different probably because of the anisotropic character of the finite reconstructed sample, but again they are of the same order of magnitude as the single phase flow ones.

Another way of analyzing D_x^* was tried by performing first a regression on S_w, second on Pe and third on K. One obtains

$$D_x^*/\overline{D} \approx 2.4\ K^{0.6} S_w^{-0.6^{Pe^{0.3}}} Pe^{0.054K} \tag{47}$$

This formula is impressive in the sense that it is unique for all the parameters which were studied, but it should be exclusively used in the range where it has been established. Formulae (45a)–(46c) seem preferable to us since the dependence in terms of the Péclet number is similar to the one obtained in single phase flow which is not true for Eq. (47).

Let us now consider the results obtained for Statoil *sd*. It should be noted that the range of parameters is also different and more restricted than in the previous situation. Here, the partition coefficient K is equal to 0.1, but the Péclet number is equal to 1, 10 and 100. The new case $Pe = 1$ was investigated for sake of completeness only. In addition to the comments which were made in the previous section, it is interesting to note that the longitudinal dispersion for $Pe = 1$ is much faster in steady state than for the two other values.

The regression analysis for the dispersion coefficients is summarized in Fig. 16. One can get the following correlations for $K = 0.1$. Again the first ones are obtained by means of an averaging over the last values (42)

$$D_x^*/\overline{D} \approx 0.61 S_w^{-0.21} Pe^{1.22} \tag{48a}$$

$$D_y^*/\overline{D} \approx S_w^{1.3} Pe^{0.8} \quad \text{and} \quad D_z^*/\overline{D} \approx S_w^{-0.8} Pe^{0.9} \tag{48b}$$

The last one is obtained by means of Eq. (44)

$$D_x^*/\overline{D} \approx 0.59 S_w^{-0.30} Pe^{1.27} \tag{49}$$

These results are interesting for themselves, but they are also interesting by comparison with the previous ones gathered in Eqs. (46a)–(46c). As discussed at the beginning of Section 4.3, the geometry of the sample is expected to have an influence on the dispersion tensor. It is seen that for the same value $K = 0.1$, the influence of saturation is different in both cases. More precisely, the dependence on the Péclet number remains more or less the same (again very close to the classical values obtained in single phase), while the influence of saturation is drastic. This could be explained in the following way. $K = 0.1$ corresponds to the case where most of the particles are in the water which is recalled to be the wetting phase. As shown in Table 2, the permeability ratio K_o/K_w is considerably larger for *sa*1865 than for *sd*. Hence, it was expected that dispersion is much larger in the Saga sample; Figs. 13 and 16a show that this is indeed the case. Hence, the sample itself has a crucial influence on the result.

Finally, it is tempting to compare the results obtained here to the ones derived in networks. Sahimi and Imdakm (1988) proposed power laws for the longitudinal dispersion as a function of the water saturation. The physical situations are actually very different. First, it is not meaningful in our computations to speak of drainage or imbibition since the saturations are fixed at the beginning and do not change with time. Second, our calculations are made over a wide range of

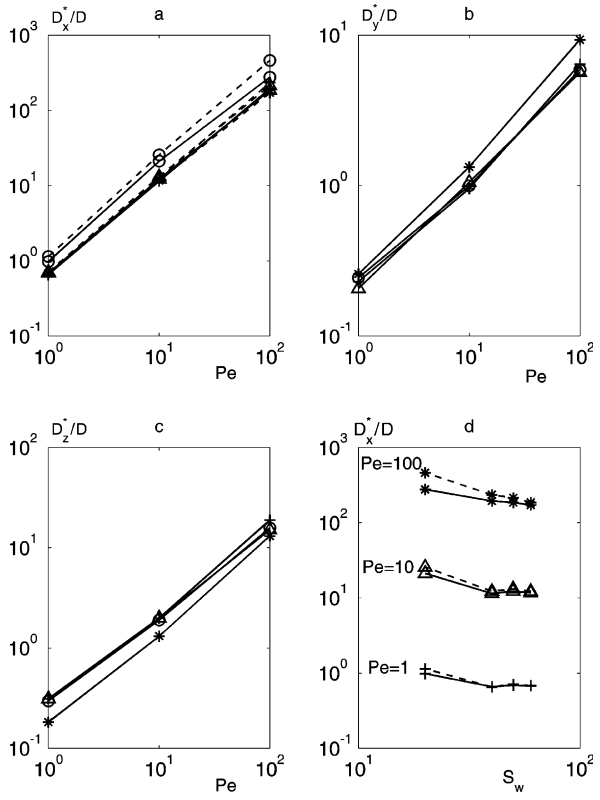

Fig. 16. Dispersion coefficients along the x-, y- and z-axes normalized by $\overline{D}$ as functions of Péclet number in the sample *Statoil sd* in (a)–(c). Conventions are: $S_w = 60\%$ (✻), $S_w = 50\%$ (△), $S_w = 40\%$ (+) and $S_w = 20\%$ (○). In (d), the longitudinal dispersion coefficients (x-axis) normalized by $\overline{D}$ as functions of S_w in the sample *Statoil sd*; conventions are: $Pe = 100$ (✻), $Pe = 10$ (△) and $Pe = 1$ (+). The solid lines correspond to the last calculated values (42), and the broken lines to the least square fit (44). Data are for $K = 0.1$.

saturations (most of them far from the percolation threshold); hence, we do not expect our results to be representative of the fractal behavior which is believed to hold close to percolation. Moreover, the studied geometries are extremely different; here, a detailed view of a few pores is given while networks present a view on the porous medium at a relatively large scale where the accent is put on the immobile phase. Hence, it is not a surprise that the results are different in both simulations.

5. Concluding remarks

The dispersion tensor has been evaluated for two samples for a number of values of the major physical parameters. The proposed correlations can be possibly used in the large scale simulators at the reservoir scale which are employed in the oil industry. Other applications in Chemical Engineering can also be envisioned.

This work can be extended in many ways. One of the most important parameters which has not been varied is wettability; as seen even in the case of a simple Poiseuille flow, the influence of

saturation may yield an increase or a decrease of dispersion and is likely to be strongly influenced by wettability.

Another important extension is when the solute is not passive, but can, for instance, interact with the walls. Such a study will be performed in a near future.

Acknowledgements

This work has been done during the European Contract Tracesim OG/00007/97/HE/NO/FR whose partial support is gratefully acknowledged. Part of the computations have been performed at CINES (Montpellier).

Appendix A

The coefficient F_d can be expressed by the following chain of formulae:

$$M = \frac{\mu_w}{\mu_o} \qquad D = \frac{D_o}{D_w} \tag{50}$$

$$B = \frac{D(KS_o + S_w)^2}{KDS_o + S_w}\left\{KMS_o^2[MS_o^2 + S_w(3 + S_o)] + S_w^2[S_w^2 + MS_o(3 + S_w)]\right\}^2 \tag{51}$$

$$\begin{aligned}
F_dB = {} & K^3M^2S_o^7\left[M^2S_o^4 + 2MS_o^3S_w + S_w^2(63 + S_o^2)\right] + DS_w^7\left[S_w^4 + 2MS_w^3S_o + M^2S_o^2(63 + S_w^2)\right] \\
& + KS_oS_w^2\left[78M^4S_o^8 + S_w^6(9DS_w^2 + 70S_o^2)\right. \\
& \quad + M^3S_o^4S_w(98DS_w^2 + 7DS_oS_w^2 + 51S_o^3 - 252S_wS_o^2) \\
& \quad - MS_oS_w^4(87DS_w^2 + 25DS_oS_w^2 + 42S_o^3 - 245S_wS_o^2) \\
& \quad \left. + M^2S_o^2S_w^2(36S_o^2 + 202S_w^2S_o^2 - 240S_wS_0^3 + 7DS_w^2(1 + 32S_o) + 23DS_w^4)\right] \\
& + K^2S_o^2S_w^2\left[78DS_w^8 + M^4S_o^6(9S_o^2 + 70DS_w^2) + MS_oS_w^4(98S_o^2 + 7S_wS_o^2 + 51DS_w^3 - 252DS_w^2S_o)\right. \\
& \quad - M^3S_o^4S_w(87S_o^2 + 25S_wS_o^2 + 42DS_w^3 - 245DS_w^2S_o) \\
& \quad \left. + M^2S_o^2S_w^2(36DS_w^2 + 202DS_o^2S_w^2 - 240DS_oS_w^3 + 7S_o^2(1 + 32S_w) + 23S_o^4)\right]
\end{aligned} \tag{52}$$

References

Adler, P.M., 1992. Porous media: geometry and transports. Butterworth/Heinemann, London.

Adler, P.M., Jacquin, C.G., Quibier, J.A., 1990. Flow in simulated porous media. Int. J. Multiphase Flow 16, 691–712.

Adler, P.M., Thovert, J.-F., 1998. Real porous media: local geometry and macroscopic properties. Appl. Mech. Rev. 51, 537–585.

Békri, S., Muller, J., Howard, J., Adler, P.M. Electrical resistivity index in multiphase flow through porous media, in preparation.

Brenner, H., 1980. Dispersion resulting from flow through spatially periodic porous media. Phil. Trans. Roy. Soc. Lond. 297, 81–133.

Chella, R., Lasseux, D., Quintard, M., 1998. Multiphase, multicomponent fluid flow in homogeneous and heterogeneous porous media. Revue de l'I.F.P. 53, 335–346.

Conca, J.L., Wright, J., 1990. Diffusion coefficient in gravel under unsaturated conditions. Water Resour. Res. 26, 1055–1066.

Delshad, M., MacAllister, D.J., Pope, G.A., Rouse, B.A., 1985. Multiphase dispersion and relative permeability measurements. Soc. Petr. Eng. J. 25, 524–534.

De Smedt, F., Wierenga, P.J., 1979. Mass transfer in porous media with immobile water. J. Hydrology 41, 59–67.

Ginzbourg, I., Adler, P.M., 1995. Surface tension models with different viscosities. Transp. Por. Media 20, 37–76.

Gunstensen, 1992. Lattice–Boltzmann studies of multiphase flow through porous media. Ph.D. thesis, MIT, Cambridge, MA.

Haga, D., Niibori, Y., Chida, T., 1999. Hydrodynamic dispersion and mass transfer in unsaturated flow. Water Resour. Res. 35, 1065–1077.

Labolle, E.M., Fogg, G.E., Tompson, A.F.B., 1996. Random-walk simulation of transport in heterogeneous porous media: local mass-conservation problem and implementation methods. Water Resour. Res. 32, 583–593.

Press, W.H., Teukolsky, S.A., Vetterling, W.T., Flannery, B.P., 1992. Numerical Recipes in Fortran 77. Cambridge University Press, Cambridge.

Sahimi, M., 1995. Flow and Transport in Porous Media and Fractured Rock. VCH, Weinheim.

Sahimi, M., Scriven, L.E., Davis, H.T., 1982. Dispersion in disordered porous media. Chem. Eng. Comm. 23, 329.

Sahimi, M., Heiba, A.A., Hughes, B.D., Scriven, L.E., Davis, H.T., 1983. Dispersion in flow through porous media, SPE paper 10969, New Orleans, LA.

Sahimi, M., Heiba, A.A., Davis, H.T., Scriven, L.E., 1986. Dispersion in flow through porous media: II. Two-phase flow. Chem. Eng. Sci. 41, 2123–2136.

Sahimi, M., Imdakm, A.O., 1988. The effect of morphological disorder on hydrodynamic dispersion in flow through porous media. J. Phys. A 21, 3833–3870.

Sallès, J., Thovert, J.-F., Delannay, R., Prevors, L., Auriault, J.-L., Adler, P.M., 1993. Taylor dispersion in porous media. Determination of the dispersion tensor. Phys. Fluids A5, 2348–2376.

Salter, S.J., Mohanty, K.K., 1982. Multiphase flow in porous media: I. Macroscopic observations and modelling. Society of Petroleum Engineers Paper 11017.

Smiles, D.E., Philip, J.R., Knight, J.H., Elrick, D.E., 1978. Hydrodynamic dispersion during absorption of water by soil. Soil Sci. Soc. Am. J. 42, 229–234.

Thovert, J.-F., Yousefian, F., Spanne, P., Jacquin, C.G., Adler, P.M., 2001. Grain reconstruction of porous media: Application to a low-porosity Fontainebleau sandstone. Phys. Rev. E 63 (061307), 1–17.

Tomadakis, M.M., Sotirchos, S.V., 1996. Transport through random arrays of conductive cylinders dispersed in a conductive matrix. J. Chem. Phys. 104, 6893–6900.